Cell Reports
Physical Science

CellPress
OPEN ACCESS

Article

Rational positioning of 3D-printed voxels to realize high-fidelity multifunctional soft-hard interfaces

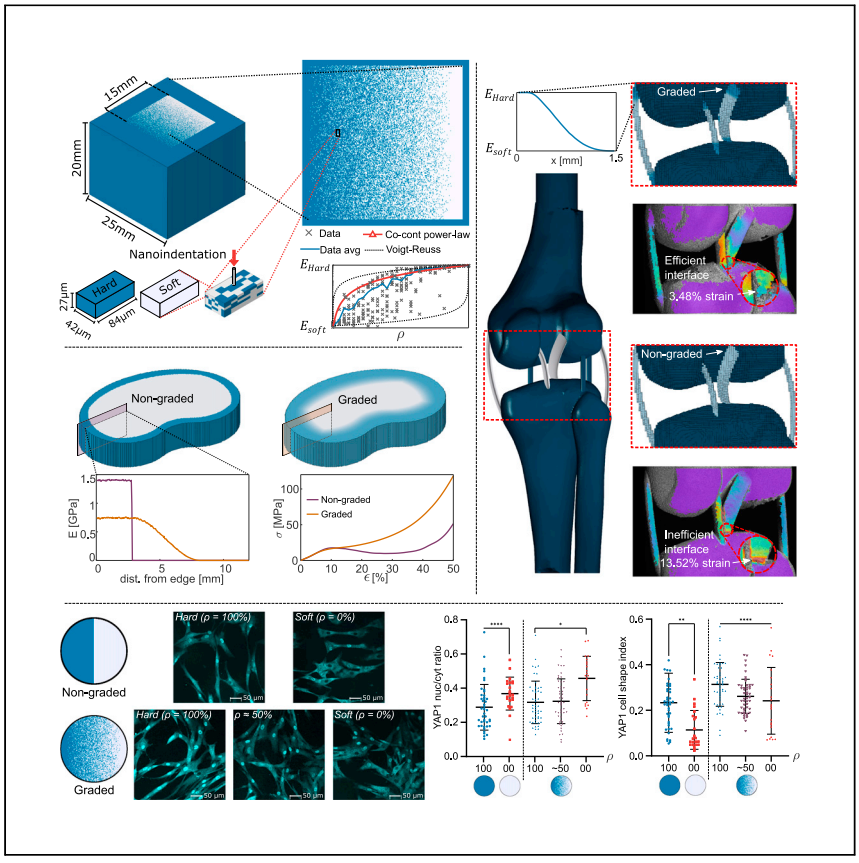

Cruz Saldívar et al. present a co-continuous power law model for rational design of functionally graded soft-hard material interfaces with precise mechanical properties. These gradients are strategically incorporated into biomimetic constructs, enhancing their strength and toughness. The effects of these interfaces on cell protein expression are also analyzed, considering their potential implementation in biomedical applications.

Mauricio Cruz Saldívar, Shima Salehi, Robin Petrus Elias Veeger, ..., Zjenja Doubrovski, Mohammad Javad Mirzaali, Amir Abbas Zadpoor

m.j.mirzaali@tudelft.nl

Highlights

Co-continuous model of voxel microarrangement to macroscale properties

Functionally graded soft-hard interfaces boost biomimetic interface performance

Effects of soft-hard constructs on cell morphology and proteins are explored

Saldívar et al., Cell Reports Physical Science 4, 101552
September 20, 2023
https://doi.org/10.1016/j.xcrp.2023.101552

Cell Reports
Physical Science

CellPress
OPEN ACCESS

Article

Rational positioning of 3D-printed voxels to realize high-fidelity multifunctional soft-hard interfaces

Mauricio Cruz Saldívar,[1] Shima Salehi,[2,3] Robin Petrus Elias Veeger,[1] Edwin Tay,[1] Michele Fenu,[4] Astrid Cantamessa,[5] Maria Klimopoulou,[1] Giuseppe Talò,[2] Matteo Moretti,[2,6,7,8] Silvia Lopa,[2] Davide Ruffoni,[5] Gerjo J.V.M. van Osch,[1,4,9] Lidy Elena Fratila-Apachitei,[1] Zjenja Doubrovski,[10] Mohammad Javad Mirzaali,[1,11,12,*] and Amir Abbas Zadpoor[1,11]

SUMMARY

Living organisms use functional gradients (FGs) to interface hard and soft materials (e.g., bone and tendon), a strategy with engineering potential. Past attempts involving hard (or soft) phase ratio variation have led to mechanical property inaccuracies because of microscale-material macroscale-property nonlinearity. This study examines 3D-printed voxels from either hard or soft phase to decode this relationship. Combining micro/macroscale experiments and finite element simulations, a power law model emerges, linking voxel arrangement to composite properties. This model guides the creation of voxel-level FG structures, resulting in two biomimetic constructs mimicking specific bone-soft tissue interfaces with superior mechanical properties. Additionally, the model studies the FG influence on murine preosteoblast and human bone marrow-derived mesenchymal stromal cell (hBMSC) morphology and protein expression, driving rational design of soft-hard interfaces in biomedical applications.

INTRODUCTION

Natural materials have developed smart design principles over millennia of evolution to interface materials with highly dissimilar mechanical properties (e.g., a hard material like bone and a soft material like cartilage or tendon).[1,2] These structural interfaces, commonly known as functional gradients (FGs), exhibit specific mechanical property transition functions (e.g., linear, power, exponential)[3,4] and are present in a vast array of biological systems, including the squid beak,[5] dentinoenamel junction,[6,7] bone-soft tissue insertion,[8–10] and byssal thread.[11] The development of advanced materials with enhanced, mutually exclusive mechanical properties (e.g., strength and toughness) is often inspired by such biomimetic design principles[12] to address challenges associated with the arising stress concentrations and the mismatch between the load-carrying capacities of both materials.[13–16]

Recent progress in polymer-based, multi-material additive manufacturing (AM; known as 3D printing)[17,18] has enabled the realization of FGs through several processes, such as material extrusion[19–23] and material jetting.[24–26] Among those techniques, voxel-based material jetting provides unparalleled freedom to design complex structures thanks to its hallmark drop-on-demand capability.[27,28] Voxel-based design of soft-hard interfaces is then akin to the positioning of soft and

[1]Department of Biomechanical Engineering, Faculty of Mechanical, Maritime, and Materials Engineering, Delft University of Technology (TU Delft), Mekelweg 2, Delft 2628 CD, the Netherlands

[2]IRCCS Istituto Ortopedico Galeazzi, Cell and Tissue Engineering Laboratory, Milan, Italy

[3]Department of Chemistry, Materials, and Chemical Engineering "Giulio Natta", Politecnico di Milano, Piazza L. da Vinci 32, 20133 Milan, Italy

[4]Department of Otorhinolaryngology, Erasmus MC, University Medical Center Rotterdam, Rotterdam, the Netherlands

[5]Mechanics of Biological and Bioinspired Materials Laboratory, Department of Aerospace and Mechanical Engineering, University of Liège, Liège, Belgium

[6]Regenerative Medicine Technologies Laboratory, Laboratories for Translational Research (LRT), Ente Ospedaliero Cantonale (EOC), Bellinzona, Switzerland

[7]Service of Orthopedics and Traumatology, Department of Surgery, EOC, Lugano, Switzerland

[8]Euler Institute, Faculty of Biomedical Sciences, USI, Lugano, Switzerland

[9]Department of Orthopedics & Sports Medicine, Erasmus MC, University Medical Center Rotterdam, Rotterdam, the Netherlands

[10]Faculty of Industrial Design Engineering (IDE), Delft University of Technology (TU Delft), Landbergstraat 15, Delft 2628 CE, the Netherlands

[11]These author contributed equally

[12]Lead contact

*Correspondence: m.j.mirzaali@tudelft.nl

https://doi.org/10.1016/j.xcrp.2023.101552

hard voxels with side lengths of, say, 42 μm next to each other to create a specific transition zone between 100% hard and 100% soft voxels. Different variations of this technique have already been used to generate hierarchical and graded constructs with improved strength and toughness.[29–31] At the macroscale, however, we usually do not care about the exact organization of voxels but would instead like to realize transition zones with specific variations in the mechanical properties. The studies performed to date have mainly analyzed such transition zones in terms of the ratio of the number of hard voxels to that of soft voxels without considering all possible permutations of hard and soft voxels.[32–34] Furthermore, it is noteworthy that the correlation between the proportions of hard and soft voxels and the resulting macroscale properties is often presumed to be linear. This assumption, however, fails to account for the markedly nonlinear nature of this correlation. This nonlinearity emerges from a multifaceted interplay of factors, including the non-linear mechanical properties of the individual materials, the complex geometrical arrangement of the different phases (somewhat similar in origin to the power law relationship between the relative density and elastic modulus of cellular materials), and the aspect ratio of the voxels. It has already been shown that such assumptions can lead to inaccurate estimations of effective mechanical behavior.[35–37]

Here, we aim to establish nonlinear models that relate the positioning of voxels to the actual values of the elastic modulus within the transition zone of FG soft-hard interfaces. We then use these models to create FG soft-hard interfaces with multiple types of functionalities. Our methodology combines experimental tools to characterize FGs through nanoindentation experiments at the microscale, quasi-static tensile tests analyzed with digital image correlation (DIC) at the macroscale, with detailed finite element models at both scales. We showcase the applications of such FG soft-hard interfaces by (1) rationally designing the soft-hard interfaces of two types of 3D-printed biomimetic constructs and (2) demonstrating that such a transition zone can be used to regulate cell behavior. The biomimetic constructs include a bone-ligament junction of the knee and the nucleus pulposus-annulus fibrosus interface of an intervertebral disk. As for the second application, property-based FGs are shown to direct the migration (i.e., durotaxis) and potential differentiation of living cells.[38–42] Here, we demonstrate that our voxel positioning approach can be used to regulate the behavior of murine preosteoblasts and human bone marrow-derived mesenchymal stromal cells (hBMSCs). Toward this aim, we analyzed the morphological differences, focal adhesion kinase (FAK) expression, subcellular localization, and yes-associated protein (YAP) nuclear translocation of primary hBMSCs across graded and non-graded specimens.

RESULTS AND DISCUSSION

Material characterization and modeling

Using voxel-based AM technology, we 3D printed two types of prism-shaped specimens with a linear gradient of hard material volume fraction (ρ) projected into their volume (Figures 1A–1C). Within these gradients, each respective value of ρ represents the ratio of the number of hard material voxels to the total number of voxels within each corresponding cross-sectional layer of the interface designs. We used VeroCyan (Stratasys, USA) UV-curable photopolymer as the hard phase for both specimens. For the soft material, however, we assigned Agilus30 Clear (Stratasys) to the first specimen type and MED625FLX (Stratasys) to the second specimen type. We tested these specimens using a nanoindentation (NI) protocol[32,43] which allowed us to interrogate multiple locations within the FG transition zones, revealing the entire elastic behavior achievable by these composites (Figures 1B–1E).

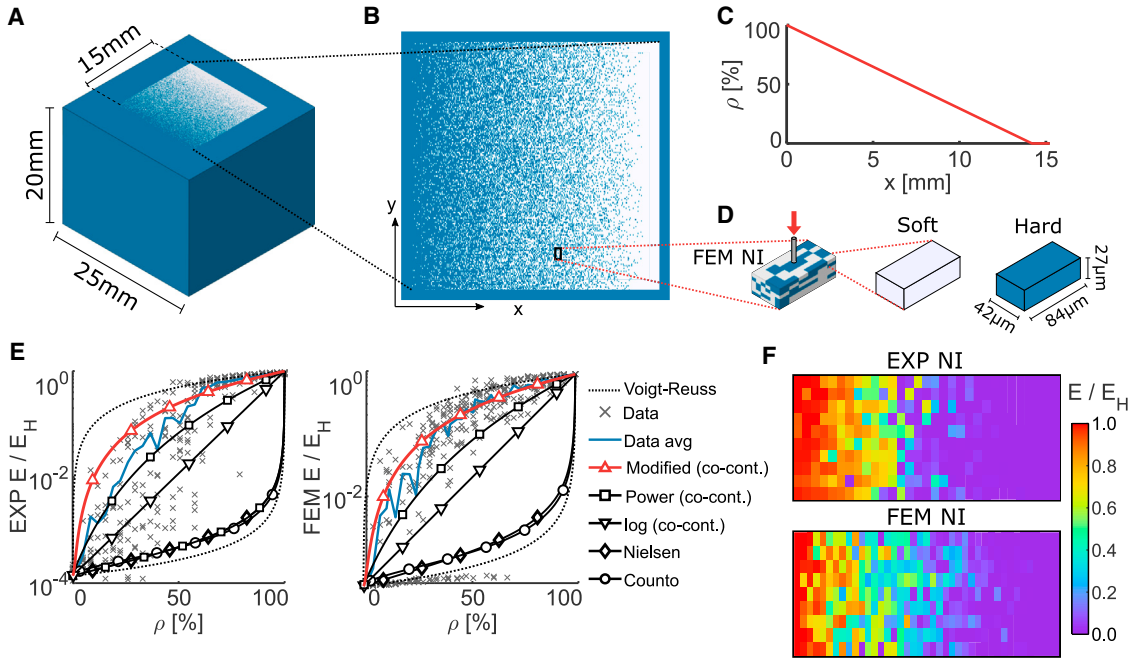

Figure 1. The initial characterization results

(A) The design of the 3D-printed specimen used for testing the properties of voxel-based composites via NI.

(B) A representative binary image of the NI specimens with a gradient of material properties projected onto their geometry.

(C) The function describing the volume fraction of the hard material, ρ, applied to the specimen for measuring the properties of these composites across their entire property space. Each $\rho(x)$ value indicates the ratio of the number of the hard material voxels to the total number of voxels in each cross-sectional layer of the interface design.

(D) An RVE extracted from a subsection of the NI specimens, used to create the FEM models of NI, accompanied by the dimensions of the voxels.

(E) The normalized elastic modulus vs. ρ and the corresponding average response (in blue) measured through NI experiment (EXP) and predicted by computational models (FEM). These values and their associated trend lines are compared with several existing models for these composites. The modified co-continuous model was found to be the most accurate.

(F) Heatmaps showing the elastic moduli measured through NI as well as the corresponding FE predictions across the FG specimens, demonstrating the linear variation of ρ. These correspond to the plots presented in (E).

Furthermore, the mechanical properties of several representative volumetric elements (RVEs) extracted from these specimens were simulated using the finite element method (FEM), which indicated good agreement between the simulations and experimental results (Figures 1D and 1E).

On average, the elastic modulus of the hard material, E_H, was 1,994.7 ($\pm$74.89) MPa. The elastic moduli of the soft materials, E_S, were 0.507 ($\pm$0.171) MPa and 5.4282 ($\pm$2.72) MPa for Agilus and MED625FLX, respectively. The elastic moduli of these materials are within the range of the elastic moduli reported for the human trabecular bone and tendon.[44–47] For the linear gradient of ρ, the experiments and simulations showed high variations in the local elastic response (Figures 1E, S1A, and S1B). The heterogeneous nature of the composites at the voxel scale caused these variations, which is the length scale probed during the NI tests (Figure 1F). Regardless of the local variations, the average response of both types of specimens showed a nonlinear transition of elastic modulus across the gradient, which contrasted with the linear transition in ρ. The actual values of the ratio of the hard voxels to the total number of voxels in 3D-printed specimens were assessed in the case of a linear $\rho(x)$ transition function and using digital microscopy (as detailed in Note S1 and Figure S2). The results of this experiment confirmed that the actual transition function is close to the prescribed transition function. Moreover, the observed behaviors of

both types of specimens and their corresponding FEM estimations were remarkably similar (Figure S1C). These two observations confirmed the validity of the obtained data and allowed us to use them as input for the mechanical characterization of such 3D-printed voxel arrangements.

Most of the predictions made by the classic models of particle-reinforced composites did not match the elastic response observed during our experiments and simulations. These models included those proposed by Nielsen et al.[48] and Counto[49] and the simplified power and logarithmic co-continuous models proposed by Davies[50] (Note S2). Among these models, the simplified power-based co-continuous model was the most accurate. While possible size effects stemming from the NI experiments could have affected our results, the high accuracy of the co-continuous model is in line with the findings of a recent study performed on non-voxelated specimens with homogeneous distributions of ρ[43]. The residual plots of this model, however, highly increased for most ρ values (Figures S1D–S1F). These high errors indicate that this version of the co-continuous model is insufficient for capturing the elastic behavior of the voxel-based composites studied here. We therefore generalized the power law-based co-continuous model as

$$E^{1/\alpha} = E_H^{1/\alpha}\rho + E_S^{1/\alpha}(1-\rho) \qquad \text{(Equation 1)}$$

where E is the elastic modulus of the composite material. Similarly, α is a power law coefficient that determines the nonlinear behavior of the composite and depends on the geometrical arrangement of the voxels, the ratio of the elastic modulus of both phases (E_H/E_S), and the particle joint probability function of the voxel arrangements.[39] After fitting this parameter with a bi-square nonlinear regression algorithm, we obtained $\alpha = 1.95$ (95% confidence interval [CI] = 1.82–2.1) and $\alpha = 1.86$ (95% CI = 1.75–1.97) for the experiments on AgilusClear and MED625FLX, respectively. Similarly, we obtained $\alpha = 1.93$ (95% CI = 1.83–2.04) for the FEM simulations. The residual of different models strongly depended on ρ. For $\rho < 25\%$, higher residuals were observed, highlighting the complexity of capturing the behavior of composites when their mechanical behavior is dominated by the soft phase. Nevertheless, the nonlinear model proposed here achieved lower residual values across the entire design space of the voxel arrangements (Figures S1D and S1E) compared with the simplified power and logarithmic co-continuous models. We therefore proceeded to the evaluation of the modified co-continuous model by designing FGs using the direct design of local elastic properties instead of designing the ratio of hard voxels to that of soft voxels.

Property by design of FGs

Generating three FGs with three different transition functions enabled us to evaluate the precision of the model (Equation 1). These FGs had linear ($E_{lin}(x)$), stepwise ($E_{ste}(x)$), and sigmoidal ($E_{sig}(x)$) functions (Figure 2), which were 3D printed using VeroCyan and AgilusClear. The shapes of these FG functions were based on those observed in the enthesis (disregarding the compliance effect caused by collagen fiber misalignment),[51] in the dentinoenamel junction (for the linear and sigmoidal FGs),[7,52] and in the distinct structures within the byssus thread and squid beaks (for the stepwise gradient).[5,53] To generate their equivalent $\rho(x)$ functions, we used the inverse of Equation 1, which has the following form:

$$\rho(x) = \frac{E(x)^{1/\alpha} - E_S^{1/\alpha}}{E_H^{1/\alpha} - E_S^{1/\alpha}} \qquad \text{(Equation 2)}$$

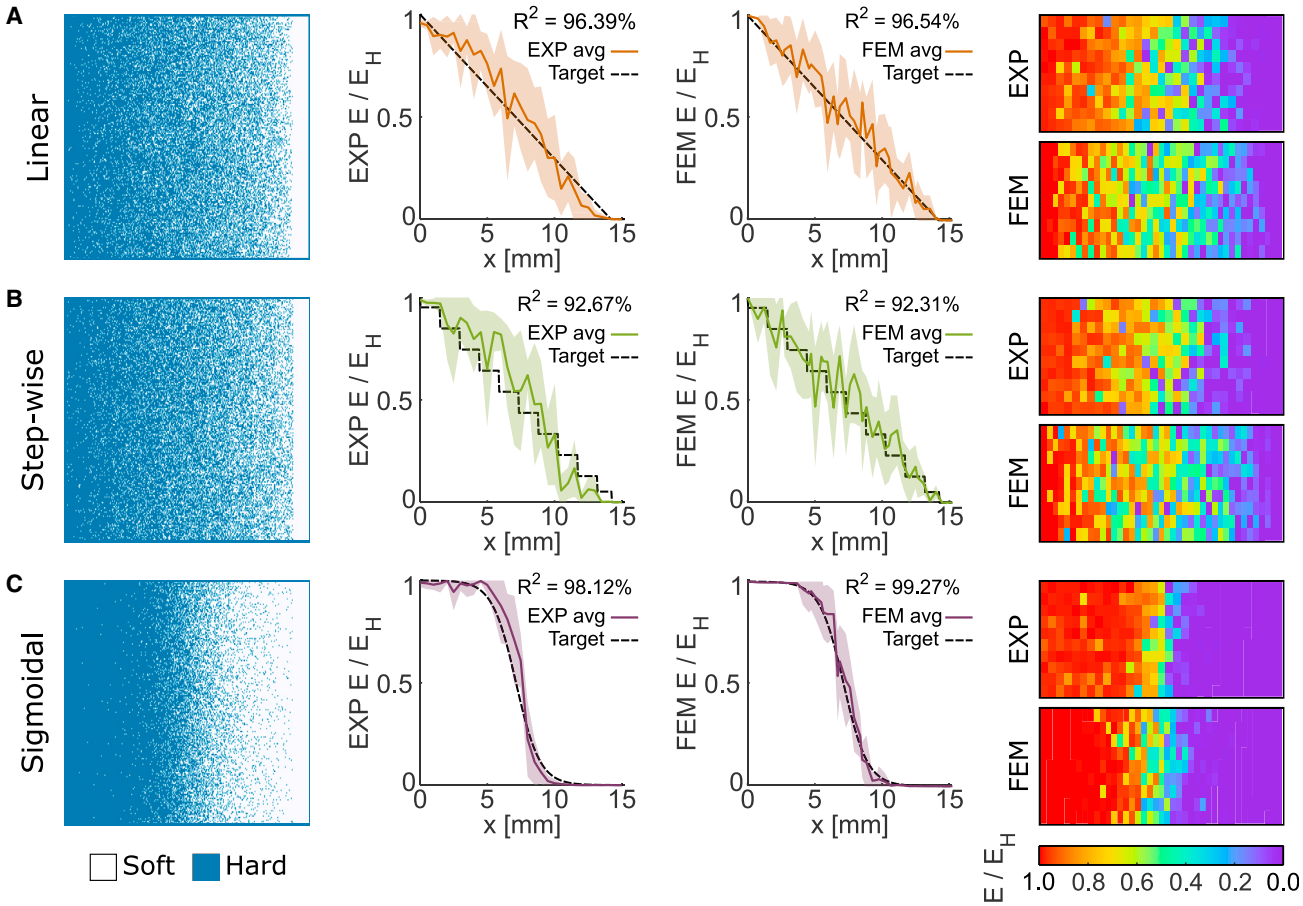

Figure 2. The measured and FEM-predicted NI results for various FG designs according to the modified co-continuous model

These tests were performed for the FGs with linear (A), stepwise (B), and sigmoidal (C) variations in the elastic modulus.

where $E(x)$ is the desired FG function. For simplicity, we chose $\alpha = 2.0$ to design these FGs because this value was within the 95% CI of the nonlinear fitting results obtained for experiments and simulations.

Similar to FGs with a linear ρ, we observed high variations in experimentally obtained and FEM-predicted values of the local elastic moduli (Figures 2A–2C). The average behavior of the FGs was, however, highly correlated with the target elastic modulus functions (i.e., $R^2 > 92\%$), particularly for the sigmoid gradients (i.e., $R^2 > 98\%$; Figure 2C). Despite the higher number of estimation points for the simulations (i.e., 1,405 simulation points per FG and 320 experimental points per FG), the average response and standard deviation of both types of characterization techniques were similar. Although many factors can complicate NI testing of polymeric materials (e.g., adhesion and viscoelasticity), the strong similarity between NI and FEM suggests that the heterogeneous nature of the voxel composites is the main cause of the high standard deviations observed here. The mean trendlines of the elastic modulus of all measurement groups resembled their corresponding designs, except for the stepwise FG group, which, despite having a high coefficient of determination ($R^2 = 92.67\%$), substantially deviated from its design function. The deviations observed in the stepwise FG group can be explained by the fact that the size of each step in that group was smaller than the observed variations in the local elastic response.

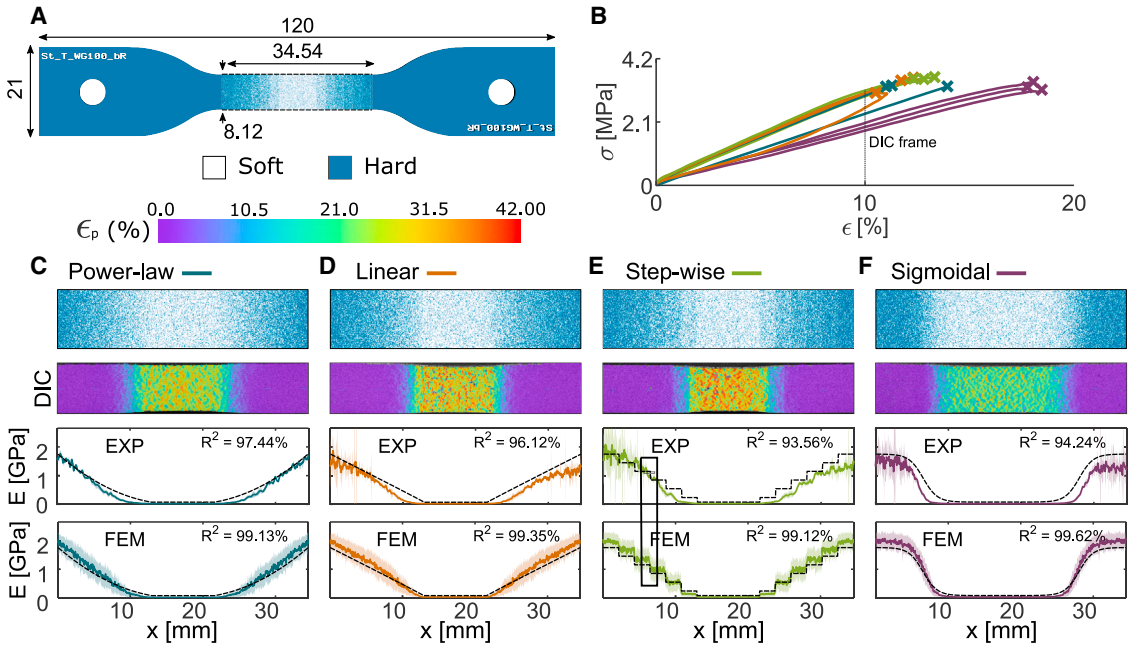

Figure 3. Additional FGs with different elastic modulus transition shapes, which were designed with the modified co-continuous model after idealizing the tensile test specimens under uniaxial deformations as systems of linear springs

(A) A representative binary image of the tensile test specimens (out-of-plane thickness = 4 mm). The gauge region was designed with four symmetric FGs. We performed DIC measurements and FEM estimations to obtain the local deformations along the gradients.

(B–F) The stress-strain curves of the experiments (B). The FGs included those with power-law (C), linear (D), stepwise (E), and sigmoidal (F) changes in the elastic modulus.

The NI experiments and their corresponding FEM simulations probed the properties of individual voxels and their close neighbors at the micrometer length scales. To assess how the microscale measurements relate to those performed at larger scales, we performed quasi-static tensile tests that measured the mechanical response of the specimens across the entire FG. We used DIC during those tests to measure the full-field strain distributions. We modeled the FGs as systems of linear springs subjected to tensile loading. To obtain the mesoscale spatial variation of the elastic modulus from the experimentally measured strains, we assumed that the local elastic modulus value along the x coordinate, $E(x)$, is equivalent to the slope between the normal stress applied to the system ($\sigma = \frac{F}{A_o}, A_o = 32.512$ mm) and the average longitudinal (engineering) strains ($\varepsilon_{p,avg}(x)$) of each cross-sectional layer of the FG ($E(x) = \sigma/\varepsilon_{p,avg}(x)$).

The stresses measured for four groups of the tensile test specimens (i.e., power law, linear, stepwise, and sigmoidal) monotonically increased with the applied strain (Figure 3B). The sigmoidal design exhibited the most compliant response. The local distributions of the elastic modulus were determined by the underlying design functions ($R^2 > 93\%$) (Figures 3C–3F). Similarly, the effective elastic moduli, $\widehat{E}$, which is the equivalent modulus of the entire interface calculated from each $E(x)$ value along the gradient, strongly correlated with the elastic moduli measured from the general stress-strain curves, E_G ($R^2 = 95.76\%$; Table S1). Despite their considerable standard deviations, the average elastic modulus across the linear, power, and sigmoid gradients followed their target elastic modulus functions, validating the possibility of generating accurate FGs. Corroboration through tensile test experiments further confirms that the NI experiments did not introduce any significant size effects,

adversely affecting the precision of our models. The mean $E(x)$ of the stepwise FG specimens, however, deviated from their corresponding design function. In fact, only the most compliant steps of these gradients were discernible. Two factors might have caused the absence of stiffer steps. First, the 6 times larger facet size of the DIC recordings compared with the voxel size has likely led to the averaging of strains in the regions where sharp step transitions were present, blurring the measured step feature. Second, partial resin mixing at the interface between the voxels may have resulted in a gradual transition of the elastic properties across the steps, similar to what other studies have suggested.[36,43,54,55] This partial resin mixing has been demonstrated to extend to up to three times the maximum voxel size (i.e., approximately 150 μm) when the interface is created prior to UV curing.[43] The build direction in the cited study aligns with the direction along which the materials presented in this study were manufactured. In contrast, none of these effects were present when simplifying the outcome from the FEM estimations into systems of linear springs. The obtained mechanical properties of the simulations showed the highest coefficients of determination in this study ($R^2 > 99\%$), and the shapes of the gradients followed the expected gradient shapes. These results confirm that the deviations in the experimental measurements were due to the imaging resolution and potential material mixing effects. Therefore, these quasi-static tensile test experiments confirm that the presented model allows for the adjustment of the actual macroscale properties of voxel-based 3D-printed FGs.

Tough biomimetic structures

We used the modified co-continuous model proposed and corroborated in the previous sections to explore the applications of FGs in the design of clinically relevant biomimetic structures. First, we considered the challenging problem of interfacing soft and hard tissues, such as ligament and bone, tendon and bone, and cartilage and bone. Toward this end, we designed two different systems of knee ligaments and performed quasi-static tension experiments and FEM simulations (Figure 4A). In the first group, we incorporated a sigmoidal FG into the design of each ligament-bone connection (Figures 4B and S4B). In the second group, however, we simply connected the soft and hard phases, effectively implementing a step function. The second group served as the control group (Figure 4C). The choice of sigmoidal functions was motivated by the results obtained in the above-presented tensile experiments and the fact that the strain distributions of these transition functions indicated a smooth transition between the hard and soft phases.

The non-graded (i.e., control) design exhibited substantial strain concentrations at the soft-hard ligament interface, particularly within the anterior cruciate ligament (ACL) region (Figure 4C). This early onset of strain concentrations resulted in non-critical cracks for low displacements (Figure S4B). Furthermore, the FEM predictions revealed that shear deformations at the ligament-bone interface cause inadequate performance of the non-graded design (Figure S4C). In contrast, the graded design showed lower strain values at the ligament-bone interfaces, indicating an improved distribution of stresses that led to a higher ultimate load before failure (Figure 4B). Moreover, the FEM simulations showed no substantial shear deformations in the graded system. These positive effects caused by the presence of FGs were reflected in the force-displacements curves of these experiments (Figure 4D). The graded structure was 1.3 times stiffer (i.e., K_g = 1.09 N/mm vs. K_{ng} = 0.84 N/mm), 1.44 times stronger (i.e., $F_{max,g}$ = 12.7 N vs. $F_{max,ng}$ = 8.82 N), and 1.55 times tougher (i.e., U_g = 180.66 mJ vs. U_{ng} = 116.77 mJ) than the non-graded design. It can therefore be concluded that decreased stress concentrations at soft-hard interfaces and reduced

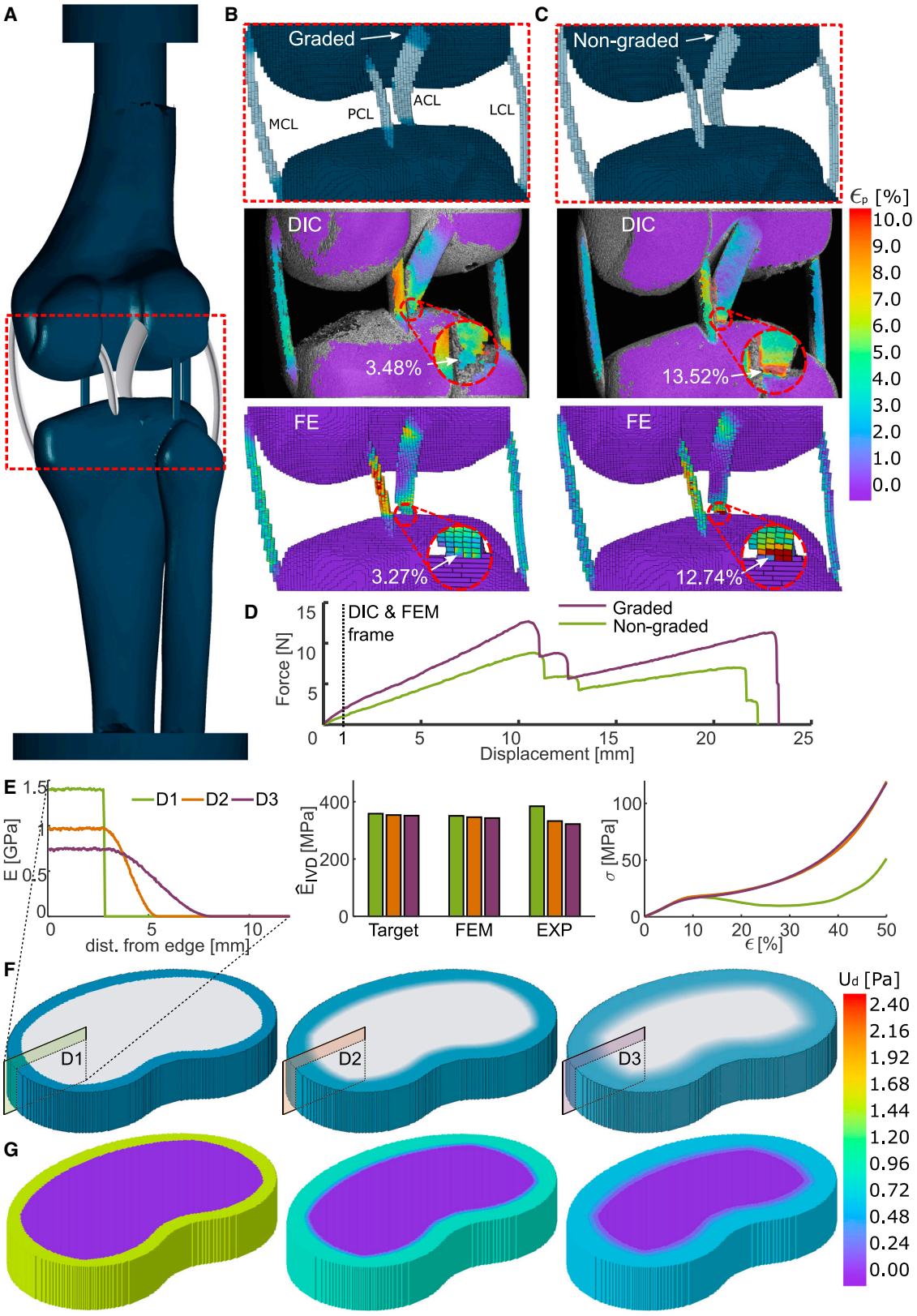
A
B
Graded
MCL
PCL
ACL
LCL
C
Non-graded
DIC
3.48%
DIC
13.52%
FE
3.27%
FE
12.74%
ϵ_p [%]
10.0
9.0
8.0
7.0
6.0
5.0
4.0
3.0
2.0
1.0
0.0
D
DIC & FEM
frame
Graded
Non-graded
Force [N]
Displacement [mm]
E
E [GPa]
D1 D2 D3
dist. from edge [mm]
$\hat{E}_{IVD}$ [MPa]
Target
FEM
EXP
σ [MPa]
ϵ [%]
F
D1
D2
D3
U_d [Pa]
2.40
2.16
1.92
1.68
1.44
1.20
0.96
0.72
0.48
0.24
0.00
G

Figure 4. A case study where we implemented several strategies of functional grading to design biomimetic devices with enhanced strength and toughness

(A) The design of a knee ligament system.

(B and C) Graded (B) and non-graded (C) versions of this knee system were defined to study the failure mechanisms of the biomimetic bone-ligament connections through DIC measurements and FEM simulations.

(D) The force-displacement curves of the graded and non-graded designs.

(E) The different sinusoidal transition functions defined for each IVD design together with the resulting mechanical properties and stress-strain curves.

(F) The representative renders of each design after projecting the elastic modulus FGs onto each lamella of the IVD.

(G) The elastic strain energy density distributions resulting from the FEM simulations performed for all designs. The specimens were subjected to quasi-static compression.

shear deformations improve the overall mechanical performance of the biomimetic FG design compared with a non-graded design.

The second biomimetic, clinically relevant construct was an intervertebral disc (IVD) with rationally designed elastic properties (Figure 4E). Although similar bioinspired structures have been introduced in the literature,[20] the gradient strategy applied in that study consisted of a stepwise FG to transfer the failure mode from the nucleus pulposus (NP) to the edge of the annulus fibrosus (AF). Their applied design methodology, however, resulted in a lower toughness compared with that of non-graded designs. To overcome this issue, we assumed that the vertical deformations of an IVD under compression occur at the same rate across its surface and that the construct fails once the lamella with the lowest ultimate strain fracture. For soft-hard voxel composites arranged in parallel as NP and AF, this failure will typically occur in the region with the highest number of stiff voxels (i.e., highest ρ value). We hypothesized that implementing an FG transition zone will reduce the interface stresses between the NP and AF. Moreover, we adjusted the maximum ρ value within the AF to be high enough to enable the construct to withstand physiological loads while remaining as low as possible to maximize its potential to store strain energy. Based on these strategies, we defined different transition functions within IVDs to increase their overall toughness while maintaining the same effective elastic response.

To demonstrate the design freedom provided by the voxels, we designed three types of specimens with three different gradient functions across the lamellae of the IVDs using sinusoidal elastic modulus functions. Within these functions, each individual value of ρ represents the ratio of the total number of hard voxels to the total number of voxels within each individual lamella. All constructs were designed to have effective elastic moduli of around 350 MPa, which we calculated using Equation 1 under the assumption that IVDs behave like systems of parallel springs. Only the last two types of IVDs included an FG transition zone (Figure 4E). After manufacturing these specimens and testing them under quasi-static compression, we compared their actual elastic moduli, which were E_{D1} = 384.3 MPa, E_{D2} = 332.6 MPa, and E_{D3} = 322.1 MPa for the first to the final design, respectively. Because the elastic properties estimated with the FEM simulations were highly similar for all designs (i.e., $E_{D1,FEM}$ = 367.5 MPa, $E_{D2,FEM}$ = 357.1 MPa, and $E_{D3,FEM}$ = 359.3 MPa), we attributed the variations in the measurements to the overestimations the corrected model yields for lower ρ values. Integrating a model correction based on the residual values of the co-continuous model may improve the precision of the designs and is suggested to be performed in future studies. Implementing a machine learning modeling approach may further minimize these errors. However, such a methodology would generally require a large number of experiments and simulations[56] and could betray the purpose of offering a simple and practical model.

The toughness values measured for both graded designs (i.e., design 2 [D2] and D3) were ≈2.4 times higher than that of the non-graded design (U_{D1} = 7.79 MPa, U_{D2} = 18.86 MPa, and U_{D3} = 19.05 MPa). The lower toughness of the non-graded design was caused by sudden separation of the AF from the NP because of their stiffness mismatch (Figure S4D), leading to a critical stress drop at ≈27% strain. In contrast, the graded designs cracked around the AF but did not show critical separation between their phases, which resulted in their continuous hardening. These outcomes support the suitability of the approach chosen for implementing FG in the design of IVDs to improve their toughness. Moreover, these experiments further corroborated the property-by-design approach proposed in the current study that allows for the free adjustment and improvement of the mechanical properties of biomimetic structures for different applications.

Regulating cell behavior

Although poly-jet 3D printing is more commonly used in biomedical research for pre-surgical planning, anatomical modeling, and the design of materials that mimic the structure and mechanical properties of tissues and other biological materials,[28] there has been insufficient research into the potential applications of these materials in tissue engineering. To address this, we extended our analyses to evaluate the potential application of our soft-hard interfaces in mechanobiological studies. This approach could leverage the extensive design possibilities of voxel-based materials for creating scaffolds that regulate or influence cellular behavior (e.g., cell morphology, migration, and stem cell differentiation) through mechanical cues (i.e., stiffness).[57] More specifically, we hypothesized that we could use the local variations in the elastic modulus of the substrates created through the rational arrangement of voxels to regulate the morphology and function of cells. The use of UV-curable photopolymers in combination with voxel-based AM techniques in the biomedical field has been limited so far because the biocompatibility of commercially available UV-curable photopolymers has only been assessed for a few cell types.[58,59] One factor limiting the extensive use of these materials is the adverse effects of their leachates on cells.[60,61] Therefore, prior to the direct seeding of cells on these materials, we assessed the cytotoxicity of materials by exposing hBMSCs and cells from a murine preosteoblast cell line (MC3T3-E1) to the material leachates (Note S6ii). We did not observe a substantial number of dead cells under any of the conditions considered here. The live/dead images, however, showed limited proliferation of MC3T3-E1 cells and BMSCs (Figures S6B and S6C). The leachates from the soft material (i.e., MED625FLX) inhibited proliferation more than those from the hard material (i.e., VeroClear) (Figures S6D and S6E). For direct cell cultures, a series of surface treatments consisting of grinding, protein coatings, and the combination thereof was first tested to improve adhesion of the cells to the 3D-printed soft-hard substrates (Note S5iii; Figures S5 and S7). We found that a combination of grinding (silicon carbide [SiC] abrasive paper, grain size = 5 μm) followed by fetal bovine serum (FBS) protein coating was the most efficient way to improve cell adherence to the substrates for hBMSCs and MC3T3-E1 cells (Figures S7D and S7E). Therefore, we implemented this surface treatment for all subsequent experiments. This strategy significantly reduces the interaction between the cells and the photopolymer, consequently mitigating the potential effects that the surface chemistry of the 3D printed materials could have on the biological response of the cells.

We first investigated the effects of the hard, soft, graded, and non-graded specimens on the morphology of hBMSCs (i.e., the area covered by each cell) after 1 day of direct culture (Figures 5A and 5B). The cell area on the non-graded

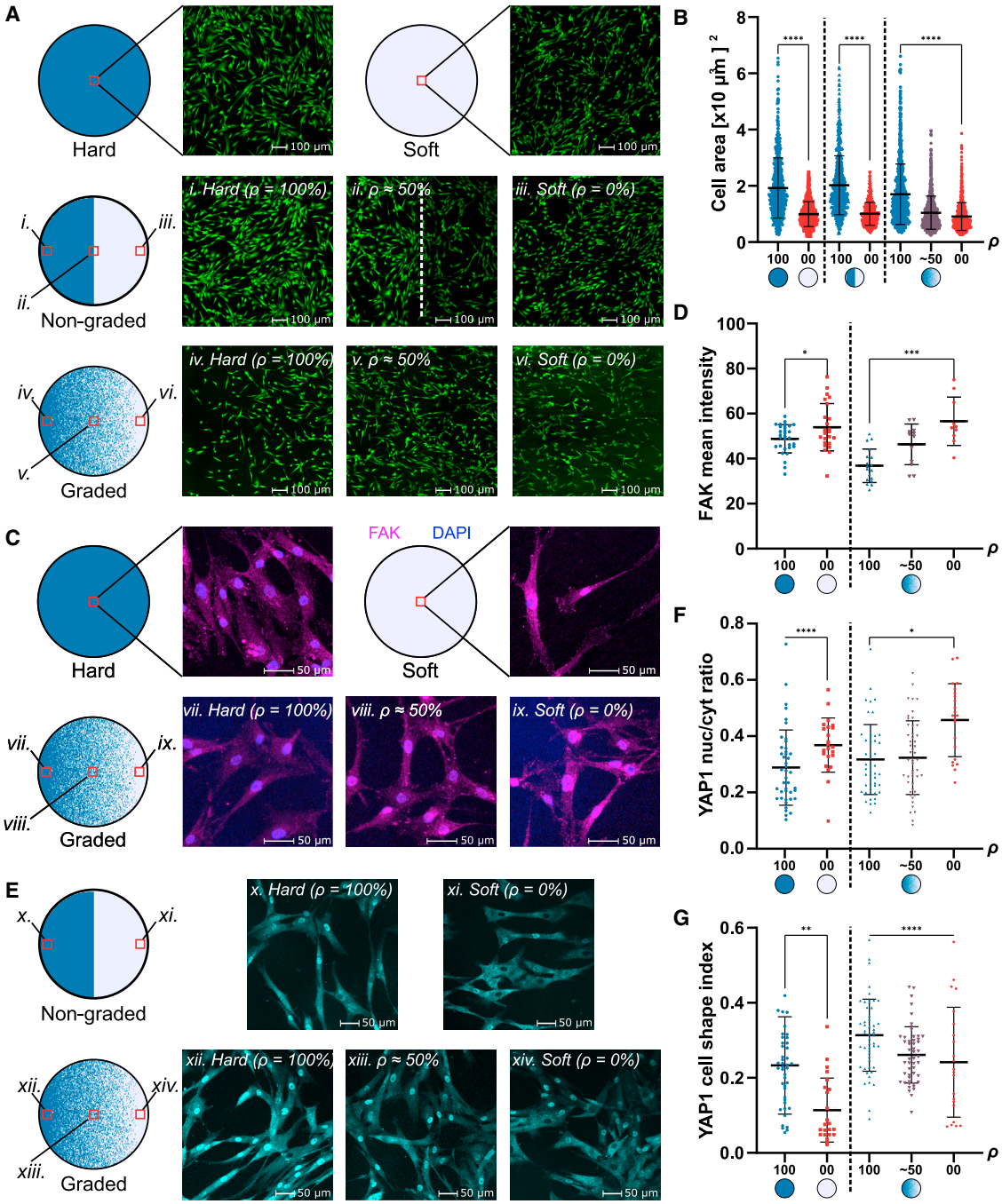

Figure 5. The results of the cell study

(A) Live/dead images corresponding to the monolithically hard and soft, non-graded, and graded specimens.

(B) A scatterplot indicating the surface area of individual cells at the specified locations across the specimens. An intermediate average surface area value was present at the center of the graded specimens.

(C) FAK immunofluorescence staining of the cells seeded on the monolithic and graded specimens.

(D) A scatterplot depicting the mean FAK intensity signal. An intermediate level (greater than the one for the hard material and less than that for the soft material) was present at the center of the graded specimens.

(E) Representative images of YAP1 (cyan, visualized via immunofluorescent staining) of cells adhering to the non-graded and graded specimens.

(F and G) Quantification of the YAP1 nuclear/cytoplasmatic ratio and CSI of the cells adhering to the specimens. The data presented in each scatterplot indicate the value per single cell. Unpaired t tests with Welch's correction were performed to compare the ranks of the extremely hard and soft results. The significance of each comparison is marked as follows: *p < 0.05, **p < 0.01, ***p < 0.001, ****p < 0.0001.

soft-hard specimens and at the extremes of the graded specimens was similar to that of their respective monolithic materials, with a clear interface observed between the hard and soft phases on the non-graded specimens (Figure 5B). The mean cell area at the center of the FG specimens was an intermediate value between the values observed for the hard and soft phases, while the values corresponding to the soft and hard extremes were similar to those observed for the non-graded specimens. This finding should be interpreted by taking into account the fact that the chemical leachate compositions of the graded and non-graded specimens were the same, meaning that the factor affecting the cell behavior is likely to be local. This consistency in the total amount of hard and soft material across all specimens, combined with the effects of the applied protein coating, suggests that the observed differences in the biological response of the cells can be primarily attributed to the stiffness of the underlying substrates.

To understand whether adhesion to the different substrates would result in differential mechano-responses, we evaluated the expression of FAK by hBMSCs seeded on the graded and monolithic specimens through immunofluorescence staining (Figure 5C). FAK is part of integrin-mediated signal transduction and participates in the formation of focal adhesions between the cells and the substrate.[62–65] The activation of FAK and the consequent signaling pathways modulate a range of cellular processes, including cytoskeletal organization, cell survival, proliferation, migration, and gene expression. By orchestrating these processes, FAK plays a pivotal role in cell adhesion, motility, and the dynamic interactions between cells and their microenvironment. Consequently, changes in FAK localization or expression levels serve as indicators of cellular responses to stiffness.[66,67] The FAK signal was distributed more homogeneously within the cells seeded on the hard material, implying a more uniform formation of focal adhesions within the hard substrate than in the soft one. As for the soft phase, the FAK signal was more intense and was concentrated around the cell nuclei (Figure S8). Again, the use of a graded substrate led to an intermediate level of FAK expression at the center of the specimens (Figure 5D). The mean intensity of FAK on the graded specimens increased gradually from the hard extreme to the soft one. Even though the regulation of FAK expression at the protein level cannot be easily attributed to single mechanical cues of the substrate, these results provide some insight into the potential effects of such soft-hard interfaces and the role of FG. More decisive conclusions, however, can only be drawn with a more thorough investigation in future studies.

Another fundamental factor in mechanosensing and mechanotransduction pathways is the YAP1/transcriptional co-activator (TAZ) factor.[68] Cell adhesion to substrates results in the assembly of actin fibers, which then transfer the cytoskeletal tension to the nuclei, opening mechanosensitive channels.[69] This process, in turn, allows YAP translocation to the nucleus, with enhanced nuclear translocation of YAP corresponding to increased tensile forces. These key downstream effectors of mechanotransduction pathways, specifically their nuclear translocation and activation, can signify a cellular response to stiffness. Specifically, a stiffer extracellular matrix (ECM) often leads to translocation of YAP/TAZ (transcriptional coactivator with a PDZ-binding motif) into the nuclei of cells.[70] We therefore evaluated the presence of this factor and assessed whether changes in the mechanical properties of the specimens regulate the nuclear translocation of the hBMSCs that were seeded on different types of specimens. The cells seeded on non-graded specimens showed a different response to the hard and soft materials (Figure 5E). The cells seeded on regions made of the hard phase had higher YAP1 nuclear-to-cytoplasmatic ratios than those seeded on the soft phase (Figure 5F). On the graded specimens, the

nuclear-to-cytoplasmatic ratio increased with the presence of the hard phase, although variations existed between cells. The observation that the nuclear-to-cytoplasmatic signal ratio is higher for stiffer materials than for more compliant ones has been reported in the literature,[71] which corroborates our results. Furthermore, the YAP staining signal in regions with mostly hard material was significantly different from those of mostly soft material for non-graded and graded specimens ($p < 0.05$). Similarly, the cell shape index was, on average, lower for cells seeded on the soft material than those seeded on the hard material for graded and non-graded specimens (Figure 5G). This observation indicates that cells residing on the soft material have a more circular shape than those on the hard material. Previous studies have shown that cells exposed to substrates with different stiffnesses tend to migrate toward regions with higher stiffness.[72] It could therefore be the case that the cells adhering to the central region of the graded specimens preferentially attach or locally migrate to the stiffer substrate, resulting in the mechanoresponse not being fully correlated with the local ratios of both phases. Nevertheless, the differences between the hard and soft phases in terms of YAP translocation to the nucleus of the cells suggest differential activation of mechanosensitive pathways, which have been shown to play a key role in controlling cell behavior, including growth, proliferation, and differentiation.[62,68,73] Again, because all substrates underwent treatments to minimize the effects of the surface chemistry of the materials on the cell response, and given the equal distribution of hard and soft materials (and, hence, similar leachate compositions), we can attribute the intermediate distribution of YAP/TAZ between the predominantly hard and mostly soft material regions to the local stiffness of the composites. These results suggest that the voxel-by-voxel manufacturing technique can be used to create customized, tunable scaffolds or substrates for studying or regulating the mechanotransduction of cells.

In this work, we developed a modified version of classic co-continuous models originally derived for particle-reinforced composites. These models aim to establish a direct relationship between the arrangement of voxels and the macroscale elastic behavior of multimaterial 3D-printed specimens with voxel-level FGs between their soft and hard phases. Using these models, FGs can be designed at the voxel level given the target function describing the variation of the elastic properties between the hard and soft materials. Our experiments and computational models indicated a high degree of correlation between the model-based designs and the actual elastic properties ($R^2 > 90\%$) of such FGs, as characterized by NI and quasi-static tension tests. We then applied the developed model to design complex biomimetic systems (i.e., knee ligaments and IVDs) with pre-programmed variations of elastic properties between their soft and hard phases. Biomimetic specimens incorporating FGs were at least 130% stronger and 140% tougher than their non-graded counterparts, indicating improved load transfer at their soft-hard interfaces. At the cell scale, our experiments supported the hypothesis that cell behavior can be guided by selective deposition of hard and soft phases in a transition region. Our results therefore pave the way for the application of graded soft-hard interfaces fabricated by voxel-level 3D printing to various areas within biomedicine (e.g., regenerative medicine and implantable medical devices). Future studies should focus on the characterization of the anisotropic response of soft-hard voxel arrangements by canvassing the space of all possible permutations of soft and hard voxels. Moreover, more extensive studies should be performed to better understand how the arrangement of voxels influences the mechanoresponse of cells. Finally, there is a need for more cytocompatible UV-curable photopolymers that can be used with the existing printers to create arbitrarily complex soft-hard interfaces at the voxel level.

EXPERIMENTAL PROCEDURES

Resource availability

Lead contact

Further information and requests for resources and materials should be directed to and will be fulfilled by the lead contact, Mohammad J. Mirzaali (m.j.mirzaali@tudelft.nl).

Materials availability

This study did not generate new unique reagents.

Data and code availability

The raw and processed data used in this study, just as the codes used to generate the composite designs and computational simulations, will be made available upon request from the lead contact.

3D printing

We fabricated all the specimens through multi-material poly-jet 3D printing (ObjetJ735 Connex3, Stratasys). This equipment allows material deposition in a "voxel-by-voxel" manner, wherein each voxel represents a microparticle to be deposited, with its shape idealized as a prism. The dimensions of these particles are constrained by the maximum resolution of the printer. Given the resolution of our printer (i.e., 600 × 300 dpi in a 27-μm layer), the minimum feasible voxel size was 42 × 84 × 27 μm^3. The resolution of the printer (i.e., 600 × 300 dpi in layers of 27 μm) enables a minimum voxel size of 42 × 84 × 27 μm^3. The material deposition was controlled using a stack of binary images, which provided a voxel-by-voxel description of the deposition coordinates of both phases. In each binary image, the white bits represent the locations where the 3D printer deposits each type of voxel, making it necessary to define, for every design, a separate stack of binary images for the soft material and another one for the hard material. Each image in a stack represents a layer of the composite with a uniform thickness of 27 μm. We prepared the binary images using a custom MATLAB (R2018b, Mathworks, USA) code, which processes the gradient functions into 3D images at resolutions compatible with those of the 3D printer. These images were then projected onto the geometries of the biomimetic devices. Subsequently, these 3D image geometries were discretized into binary image files. When the stacks of images were ready, they were processed for manufacturing using GrabCAD Print (Stratasys). For most of the mechanical experiments, the hard and soft phases were made from the UV-curable photopolymers VeroCyan (RGD841, Stratasys) and Agilus30 Clear (FLX935, Stratasys), respectively. The biocompatible MED625FLX (Stratasys) was used as the soft phase in a single NI specimen with a linear ρ gradient and for all biological experiments. Further details regarding the fabrication process are presented below.

NI

Specimen design

To create the FGs, we discretized their $\rho(x)$ functions across the printing direction (x direction; Figure 1A) at the maximum voxel resolution (i.e., 42 μm/voxel). For each of the 355 points of the $\rho(x)$ function, we calculated the total number of hard voxels (n_H) required to achieve their respective $\rho(x)$ value (i.e., $n_H(x) = \rho(x) \times n_{layer}$, $n_{layer} = 177 \times 740$ voxels^2) and randomly distributed them over the voxels with the same x coordinate. We projected the resulting design at the center of cubic geometries (25 × 25 × 20 mm^3) with the hard phase bounding the FGs. Additionally, the final 1 mm of every design was assigned ρ = 0%, which served as a reference for the NI procedure. The shape of the initial FG was a linear function of ρ ($\rho_{lin}(x) = -x/L_G + 100$), which was printed twice: once with Agilus Clear as the soft phase and

then with MED625FLX as the soft phase. These specimens were used for material characterization. Later, we defined three specimens with different elastic modulus functions. Their shapes were linear ($E_{lin}(x) = -(E_H - E_S)x/L_G + E_H$), stepwise (i.e., $E_{step}(x)$, similar to $E_{lin}(x)$ but discretized in nine steps), and sigmoidal ($E_{sig}(x) = (E_H - E_S)/(1 + \exp(d(x - L_G/2))) + E_S, d = 8/9\ \text{mm}^{-1}$), all with a gradient length of L_G = 14.8 mm. These latter specimens were used for validation. We used a water jet system (Genie 600, Gemini Cleaning Systems, UK) at 12 bar to remove the support material from the specimens.

NI experiments

We used a TI 950 Triboindenter (Bruker, US) with a diamond conospherical probe with a tip radius of 20 μm to perform the NI experiments. We followed a previously described polishing and NI protocol.[32,43] The NIs were performed in a grid of 33 points along the *x* direction and 10 points along the *y* direction, yielding 330 experimental data points per FG. For each FG, the initial position of the nanoindenter was placed at the edge between the regions with only soft and only hard voxels. The distance between successive test points was 500 μm in both directions. Whenever the pull-off forces were >5% of the maximum load, we obtained the reduced elastic modulus (E_r) of each point using the Johnson-Kendall-Roberts (JKR) model.[74] For cases where the pull-off forces were <5% of the maximum load, we used the Oliver-Pharr model.[75] Finally, we calculated the associated elastic moduli (i.e., $E(x) \approx E_r(1 - \nu(x)^2)$) by assuming the Poisson's ratio along the gradient ($\nu(x)$) to be described by the rule of mixtures between the hard and soft phases (i.e., $\nu(x) = \nu_H \rho(x) + (1 - \rho(x))\nu_S, \nu_H = 0.4, \nu_S = 0.495$). For the linear ρ FG results, we compared the resulting elastic modulus functions against predictions made by several existing models for particle-reinforced composites, including those proposed by Nielsen et al.[48] and Counto[49] and both simplified co-continuous models proposed by Davies[50] (i.e., power and logarithmic models). Comparison with these equations, which are described in detail in Note S2, allowed us to obtain the most accurate model that fits our data. For obtaining the α value of the modified co-continuous model (Equation 1), we performed a bi-square nonlinear regression between all available elastic moduli of the linear ρ function and their corresponding values of the hard voxel volume fraction. For the linear, stepwise, and sigmoid $E(x)$ functions, we calculated the coefficients of determination (ordinary R^2 values) between the measured data and the designed functions to validate the accuracy of the selected characterization model.

FEM simulations of the NI experiments

We used a commercial software suite (Abaqus Standard v.6.14, Dassault Systèmes Simulia, France) to perform the FEM simulations of the NI experiments. Each model was built using a grid of RVEs taken from 39 positions along the *x* direction and 9 positions along the *y* direction (Figure 1B). After a mesh convergence study (Note S3; Figure S3A), each RVE included a matrix of 6 × 6×6 voxels. Each voxel was discretized using a cluster of 6 × 6×6 linear hexahedral elements (C3D8H). We simplified the indenter probe as a cylindrical rigid body defined as a rigid analytic shell with a radius (R_p) of 6.25 μm. We performed four simulations per RVE to account for the nanoindenter position during the tests. In these simulations, the indenter was randomly positioned above the centermost half of the mesh. This process resulted in 1,404 simulations per FG. We defined the elastic properties of every hard (i.e., E_H = 2000 MPa, ν_H = 0.4) and soft (i.e., E_S = 0.87 MPa, ν_S = 0.495) element based on the NI experimental results. The Poisson's ratio of both materials and the elastic modulus of the soft phase were obtained from the quasi-static tensile tests

performed on monolithic materials (Figures S3B and S3C). We constrained all degrees of freedom of the bottom and lateral regions of every mesh. For the probe, we prescribed an indentation depth (h) of 1 μm and recorded its respective reaction forces (RFs) for each simulation. We calculated the reduced elastic modulus ($E_r = \sqrt{\pi}\, RF/(2\, h\, \sqrt{A_p}), A_p = \pi\, R_p^2$) and used the Poisson's ratios of the RVEs (i.e., $\nu = \nu_H \rho(x) + \nu_S(1 - \rho(x))$) to estimate the elastic modulus ($E = E_r\,(1 - \nu(x)^2)$) for every simulation. To plot the variation of the elastic modulus across the length of each FG design, we used a combination of the overall ρ value of each RVE and the corresponding value of the estimated elastic modulus, E.

Tensile tests

Tensile mechanical tests

First, we prepared monolithic specimens made of only hard and only soft voxels according to the description of type IV specimens in the American Society for Testing and Materials (ASTM) D638-14 standard.[76] These specimens allowed us to characterize the elastic properties of these materials when loaded in the printing direction. Furthermore, we designed four elastic modulus FGs to validate the accuracy of the corrected characterization models under quasi-static tensile conditions. The shapes of the FGs were a power law (i.e., $E_{pow}(x) = (E_{max} - E_{min})((L_G - x)/L_G)^2 + E_{min}$), linear (i.e., $E_{lin}(x) = -(E_{max} - E_{min})/L_G + E_{max}$), step (i.e., $E_{step}(x)$, similar to $E_{lin}(x)$ but discretized using 9 equally spaced steps), and sigmoid ($E_{sig}(x) = (E_{max} - E_{min})/(1 + \exp(d(x - L_G/2))) + E_{min}, d = 8/9\ \ \mathrm{mm}^{-1}$), all with L_G = 12.2 mm. We symmetrically projected these FGs onto the gauge region of the specimens, with their centermost 8.13 mm defined by E_{min} (Figure 3A). We defined E_{max} = 1,750 MPa and E_{min} = 75 MPa for all of these FGs. The $\rho(x)$ functions were obtained using Equation 2 with α = 2, E_S = 0.87 MPa, and E_H = 2650 MPa (E_H and E_S were obtained from tensile tests performed on monolithic specimens). We manufactured each design threefold and removed the support material using a water jet system (Genie 600, Gemini Cleaning Systems) at 12 bar. We tested the specimens using an LR5K mechanical testing machine (Lloyd, USA) with a 5-kN load cell at a rate of 2 mm × min^{-1}. We recorded the local deformations of the specimens during the tests using a DIC system (Q-400 2× 12 MPixel, Limess, Krefeld, Germany) that captured the surface of the specimens with a frequency of 1 Hz. These measurements required applying a black dot speckle pattern over a white paint background on each specimen. We calculated the first principal (true) strain distributions with the Instra 4D v.4.6 (Danted Dynamics, Skovunde, Denmark) software and the DIC measurements. Furthermore, we generated the general stress-strain curves across time (t) using the engineering stress ($\sigma(t) = f(t)/A_0, A_0 = 32.512\ \mathrm{mm}^2$) and engineering strain vectors, $\varepsilon(t)$, measured using a digital extensometer in Instra 4D. From these curves, we measured the general elastic modulus of each tensile test specimen, E_G, from the slope of a fitted polynomial of order one. To calculate the elastic modulus along the x direction, $E(x)$, we fitted polynomials using the average longitudinal (engineering) strains ($\varepsilon_{avg}(x,t)$) of each x position and the engineering stress vectors. All slopes were obtained between stresses of 0.2 and 15 MPa. We then averaged the $E(x)$ results for three repetitions of each FG and calculated the corresponding coefficients of determinations (ordinary R^2 values) between the experimental results and the FG designs. We further validated this method of measuring $E(x)$ by calculating the effective elastic modulus $\widehat{E}$ of each test using the equivalent equation for the systems of linear springs ($\widehat{E} = W_G\left(\int_0^{W_G} dx/E(x)\right)^{-1}$, where W_G is the total length of the DIC recording region) and by comparing them with the elastic moduli measured from the general stress-strain curves (E_G).

FEM simulations of the tensile tests on FG specimens

We modeled one-half of the gauge section of the tensile test specimens with a cross-section of 24 × 24 voxels and discretized them with linear hexahedral elements (C3D8H). The resulting meshes consisted of 235,008 elements. Given these considerations, we prescribed symmetric boundary conditions at the symmetric end (i.e., at the center plane of the soft region) of the design and at two of its lateral surfaces. We also prescribed a uniaxial displacement of 0.26 mm at the hard end of the mesh (equivalent to 1.5% uniaxial strain) while restraining its remaining degrees of freedom. The elastic properties were defined using the tensile test data obtained using the monolithic specimens (i.e., E_H = 2650 MPa, ν = 0.4 for the hard phase and E_S = 0.87 MPa, ν_S = 0.495 for the soft phase). After processing the simulations, we extracted the RFs at the hard end of the FG and the main principal strains at the centroid of every element of the mesh. We performed the same procedure described for the experimental tensile tests to obtain the estimated $E(x)$ functions of every FG and to calculate their coefficients of determination (ordinary R^2- values) vs. the designed functions.

Design, testing, and FEM simulation of knee ligament systems

The geometry of the knee ligament system was adapted from an open-source computer-aided design (CAD) database.[77] It consisted of a femur, a tibia, and a fibula (153 mm long) with the respective ACL (15 mm long), posterior cruciate ligament (PCL; 20 mm long), lateral collateral ligament (LCL; 30 mm long), and medial collateral ligament (MCL; 35 mm long) (Figure 5A). From this assembly, we generated two designs. The first one had FGs between the bone-ligament interfaces. The second design, which worked as our control, was not graded and had abrupt material transitions. The material assignment of both structures was generated with MATLAB (R218b, Mathworks). The FGs of the first design had a sigmoid transition function with L_G = 1.5 mm. To attach the structures to the tensile testing machine, we integrated three cylinders between the femur and tibia regions, which we cut before testing. After removing the support material with a water jet (Genie 600, Gemini Cleaning Systems) at 12 bar, we applied a black dot speckle pattern to a white paint background to measure the system's deformations with the DIC system. We tested the assemblies under the same conditions as the tensile tests. Furthermore, we built FEM models of both test configurations after reducing their voxel resolution to grayscale RVEs covering 6 × 6 × 6 of the original voxels. We discretized each RVE as a single element (C3D8) and assigned its mechanical properties based on its average ρ after using Equation 1. We constrained all degrees of freedom at the bottom surface of the tibial bone. Similarly, we constrained all degrees of freedom at the top surface of the femur mesh, except for the vertical displacement, which was defined as 1 mm. We compared the resulting strain fields of these simulations with the results of the DIC measurements.

Design, testing, and FEM simulation of graded IVDs

We based the dimensions of the IVDs on the L4L5 disc[78] and generated the design with SolidWorks 2021 SP2.0 (Dassault Systèmes). The major axis was 49.7 mm, with a minor axis of 31.83 mm and a height of 8.42 mm. After voxelizing the design using MATLAB R2018, we generated three different IVD systems. These IVDs had different sinusoidal FG functions that connected the AF and NP regions (Note S4). To discretize these functions, we partitioned the IVDs into concentric lamellae and assigned their respective ρ value. The three designs were calculated to have an equivalent elastic modulus of 350 MPa after considering the IVDs as systems of parallel springs (Figure 4E). After printing these designs and removing the support material with a water jet (Genie 600, Gemini Cleaning Systems) at 12 bar, we tested them under uniaxial compression with a mechanical testing machine (load cell = 100 kN, Z100,

Zwick, Germany) and using a stroke rate of 2 mm × min^{-1}. The stresses and strains were calculated from the load cell readings and the corresponding cross-head displacements. To obtain more accurate elastic modulus (E_{IVD}) values, we printed additional specimens of each design and tested them with the same LR5K testing machine (5-kN load cell). The local deformations were measured using the above-described DIC system. Based on these results, we defined a digital extensometer around the centermost part of the IVDs to calculate the average vertical strains of each specimen. Then, we obtained E_{IVD} from the slope of the linear region of the stress-strain recordings (i.e., between the stress values σ = 3 MPa and 4 MPa). We compared these measurements with the values predicted by the FE models of these designs, which were built using the same discretization conditions as for the knee ligament constructs. However, each RVE had 3 × 3 × 3 voxels, and the simulations were performed under a uniaxial compression equivalent to 5% strain.

Cell culture experiments

3D-printed specimens

We designed and 3D printed four types of disk-shaped specimens (i.e., with a diameter of 9.75 mm and an out-of-plane thickness of 2 mm) to perform the cell culture experiments. Two of these were made of purely hard (i.e., VeroClear, Stratasys) and purely soft (i.e., MED625FLX, Stratasys) materials. The other two were designed as non-graded and graded multimaterial configurations. The non-graded design had a sharp interface at the center of the disk, with one side of the specimen made only of the hard voxels and the other printed from the soft voxels. The graded design had a linear ρ FG analogous to the FG of the initial NI characterizations.

Specimen preparation for direct cell seeding

After 3D printing the specimens, the support material was removed from the printed specimens using a water jet (Genie 600, Gemini Cleaning Systems) at 12 bar. Further removal of support material residuals was done by submerging the specimens in isopropanol under sonication (5510, Branson, UK) for 30 min. Thereafter, the specimens were surface treated by grinding and subsequent FBS coatings, as described in Note S6.

Cell viability and FAK analyses

Human BMSCs (Lonza, 19TL155677) were thawed and plated at 6,000 cells/cm^2 in an expansion culture medium containing basal alpha minimum essential medium (α-MEM; 22571), 10% (v/v) FBS (HyClone), 100 U/mL penicillin, 100 μg/mL streptomycin, and 10 mM 4-(2-hydroxyethyl)-1-piperazineethanesulfonic acid (HEPES), supplemented with 1 ng/mL of fibroblast growth factor 2 (all from Thermo Fisher Scientific, Waltham, MA, USA). The culture medium was renewed every 2 days. Upon reaching 80% confluency, the cells were detached from plastic using 0.05% trypsin-EDTA solution (Thermo Fisher Scientific). At passage three, 104 BMSCs suspended in 300 μL (33,000 cells/mL) were seeded directly onto the specimens and were kept at 37°C in a 5% CO_2 incubator for 2 h. Then, the medium was changed to remove the unadhered cells. The specimens were kept in culture for 48 h, with medium renewal after 24 h, and were then harvested for cell viability and FAK analysis.

Cell viability was analyzed using live/dead assays (LIVE/DEAD Viability/Cytotoxicity Kit, Thermo Fisher Scientific). After removing the culture medium and washing the cells twice with phosphate-buffered saline (PBS; Thermo Fisher Scientific), we stained the live and dead cells using 2 mM ethidium homodimer-1 and 5 mM calcein-AM for 15 min at room temperature. Then, the solution was removed, and the cells were washed twice with PBS. Finally, the cells were imaged with a ZOE fluorescent cell imager (Bio-Rad, the Netherlands).

For the FAK immunofluorescence staining, BMSCs were fixed for 10 min with 2% paraformaldehyde and washed twice with PBS. The cells were permeabilized with 0.5% Triton X-100 for 5 min, followed by 1-h blocking of non-specific binding sites with PBS with 5% (v/v) bovine serum albumin (BSA) (Sigma-Aldrich, St. Louis, MO, USA) at room temperature. The cells were then incubated with FAK primary mouse monoclonal antibody (1:200, AHO1272, Thermo Fisher Scientific) dissolved in PBS with 1% BSA for 1 h at room temperature. The specimens were subsequently washed three times with PBS and incubated with a secondary fluorescent goat anti-mouse Alexa Fluor 647 conjugate (A21235, Thermo Fisher Scientific) at a dilution of 1:1,000 in a blocking solution of PBS containing 1% BSA together with 300 nM DAPI nucleus stain. After 1 h of incubation at room temperature, the specimens were washed with PBS and stored at 4°C until the images were taken using a confocal microscope (Leica-SP8, Leica, Germany) using a 20× air-dry objective.

YAP analysis

hBMSCs isolated from the surplus bone chips from the iliac crest of a donor (age, 9 years; male) undergoing alveolar bone graft surgery were obtained with the approval from the medical ethics committee of Erasmus MC (MEC-2014-16). The cells were isolated through plastic adherence and expanded in α-MEM supplemented with 10% (v/v) FBS, 1.5 μg/mL Fungizone, 50 μg/mL gentamicin (all from Thermo Fisher Scientific), 25 μg/mL L-ascorbic acid 2-phosphate (Sigma-Aldrich), and 1 ng/mL fibroblast growth factor 2 (Instruchemie, Delfzjil, the Netherlands) in a humidified atmosphere at 37°C with 5% of CO_2 up to passage 4. 104 BMSCs suspended in 300 μL (33,000 cells/mL) were seeded directly onto the specimens and kept at 37°C in a 5% CO_2 incubator. The samples were kept in culture for 48 h in culture medium containing α -MEM supplemented with 10% (v/v) of FBS, 1.5 μg/mL Fungizone, 50 μg/mL gentamicin, and 25 μg/mL L-ascorbic acid 2-phosphate.

For YAP immunofluorescence staining, the cells were fixated using 4% paraformaldehyde (Boomlap, Meppel, the Netherlands) for 10 min, washed twice with PBS, and kept in PBS at 4°C until further processing. To stain the cells, they were permeabilized with 0.5% Triton X-100 for 5 min, followed by blocking the non-specific binding sites with PBS supplemented with 1% (v/v) BSA (Sigma-Aldrich). The cells were then incubated with rabbit anti-YAP1 primary antibody (1:500, AB52771; Abcam, Cambridge, UK) dissolved in PBS with 1% BSA for 1 h. A rabbit immunoglobulin G (IgG) isotype (X0903; Agilent Technologies, Santa Clara, CA, USA) was used as the negative control. The specimens were washed three times with PBS and incubated with goat anti-rabbit secondary fluorescent antibody (1:1,000, AB150077; Abcam) dissolved in PBS with 1% BSA for 1 h at room temperature. Nucleus staining was done using Hoechst dye 33542 (1:2,000; Thermo Fisher Scientific) for 5 min, followed by two washing steps with PBS 1% with BSA. Finally, the specimens were kept in PBS and stored in the dark at 4°C until imaging. Images were taken with a confocal microscope (Leica-SP8, Leica) using a 20× air-dry objective.

Image analysis

All images were processed using Fiji (v.1.53q, a distribution of ImageJ2, USA). The quantification of the mean FAK and YAP signal intensity as well as the cell surface area and shape index was performed using an in-house macro for the Fiji software. To analyze the surface area of the cells based on the live/dead images, the borders of the cells were automatically selected based on thresholding. The same process was applied manually for the FAK and YAP signal intensity analyses because the background signal was too high. The cell shape index (CSI) was calculated from the cytoplasm results of every manually selected cell from the YAP analysis. This

index was defined as $CSI = \frac{4\pi A}{P^2}$, where A and P represent the area and perimeter of the cell, respectively. A CSI value of 1 indicates that the cell is entirely circular, while 0 indicates a straight line. The scatterplots of the cell area were created based on 400–500 selected cells for each experimental condition. For the FAK and YAP plots, at least 10 cells were selected to perform the analysis, mainly among the isolated cells that were not overlapping or connected to other cells.

Statistical analyses of images

Statistical analyses were performed for the cell surface area, FAK mean signal intensity, and YAP1 nucleus-to-cytoplasm ratio using Prism (v.9.4.1, GraphPad, USA). Scatterplots were obtained from each corresponding evaluation, where the respective mean and standard deviations were included. For every analysis, we performed unpaired t tests without assuming equal standard deviations (i.e., Welch's correction) to compare the ranks of the results corresponding to the hard and soft materials. We indicated the significance of each comparison as follows: *$p < 0.05$, **$p < 0.01$, ***$p < 0.001$, and ****$p < 0.0001$.

SUPPLEMENTAL INFORMATION

Supplemental information can be found online at https://doi.org/10.1016/j.xcrp.2023.101552.

ACKNOWLEDGMENTS

M.J.M. acknowledges funding from NWO-Domain Science XS (with code no. OCENW.XS22.2.044) and the Idea Generator (NWA-IDG) research program with code nos. NWA.1228.192.206 and NWA.1228.192.228. This project was partially funded by Open Mind Convergence and the Dutch Medical Delta project: Reg4Med. This research was supported by the scholarship program for foreign studies no. 498307 granted by the Mexican National Council of Science and Technology (CONACYT). S.S., S.L., G.T., and M.M. acknowledge funding from the Italian Ministry of Health (Ricerca Corrente). This research was conducted on a Stratasys Objet350 Connex3 printer through the Voxel Print Research Program. This program is an exclusive partnership with Stratasys Education that enhances the value of 3D printing as a powerful platform for experimentation, discovery, and innovation; for more information, contact academic.research@stratasys.com. We kindly acknowledge Quentin Grossman from the University of Liege for helping with sample polishing prior to nanoindentation. The authors express thanks to Janneke Witte-Bouma and Dr. Eric Farrell from the Department of Oral and Maxillofacial Surgery, Erasmus MC, University Medical Center Rotterdam, the Netherlands, for contributing to the isolation and expansion of cells.

AUTHOR CONTRIBUTIONS

M.J.M. and M.C.S. designed the research. M.C.S. and R.P.E.V. performed numerical simulations of nanoindentation tests. R.P.E.V., M.C.S., Z.D., and M.J.M. designed and prepared specimens for nanoindentation tests, uniaxial tensile tests, knee ligament systems, and intervertebral disc models. A.C., R.P.E.V., and D.R. performed nanoindentation tests and the data analysis thereafter. M.C.S. performed tensile tests of the graded specimens, knee ligament systems, intervertebral disc, and DIC measurements. E.T. performed microscopic analysis for the linear gradient verification. M.C.S., M.J.M., S.S., M.K., and M.F. performed specimen preparation for cell culture experiments. S.S., M.K., and M.F. performed direct cell seeding experiments. S.S., M.M., S.L., M.K., and L.E.F-.A. performed cell viability and FAK analysis. M.F. and G.J.V.M.v.O. performed YAP analysis. M.C.S., S.S., M.F., G.T., M.M., S.L.,

G.J.V.M.v.O., L.E.F-.A., and M.J.M. performed image analyses and data interpretation for cell studies. M.C.S. and S.S. performed statistical analyses. M.C.S., Z.D., D.R., M.J.M., and A.A.Z performed the data analyses and interpretation of the mechanical test experiments. M.J.M. and A.A.Z. supervised the work. M.C.S., S.S., M.F., M.J.M., and A.A.Z. wrote the first draft of the manuscript. All the authors critically revised the manuscript for its intellectual content and approved the manuscript.

DECLARATION OF INTERESTS

The authors declare no competing interests.

Received: February 13, 2023
Revised: July 4, 2023
Accepted: August 2, 2023
Published: August 21, 2023

REFERENCES

1. Naleway, S.E., Porter, M.M., McKittrick, J., and Meyers, M.A. (2015). Structural Design Elements in Biological Materials: Application to Bioinspiration. Adv. Mater. *27*, 5455–5476. https://doi.org/10.1002/adma.201502403.

2. Liu, Z., Meyers, M.A., Zhang, Z., and Ritchie, R.O. (2017). Functional Gradients and Heterogeneities in Biological Materials: Design Principles, Functions, and Bioinspired Applications (Elsevier Ltd)). https://doi.org/10.1016/j.pmatsci.2017.04.013.

3. Giannakopoulos, A.E., and Suresh, S. (1997). Indentation of solids with gradients in elastic properties: Part I. Point force. Int. J. Solids Struct. *34*, 2357–2392. https://doi.org/10.1016/S0020-7683(96)00171-0.

4. Suresh, S. (2001). Graded materials for resistance to contact deformation and damage. Science (80- *292*, 2447–2451. https://doi.org/10.1126/SCIENCE.1059716/ASSET/04A3403E-4A23-4FDA-9FB3-407247772966/ASSETS/GRAPHIC/SE2519535004.JPEG.

5. Miserez, A., Schneberk, T., Sun, C., Zok, F.W., and Waite, J.H. (2008). The Transition from Stiff to Compliant Materials in Squid Beaks. Science *319*, 1816–1819. https://doi.org/10.1126/SCIENCE.1154117.

6. Marshall, G.W., Balooch, M., Gallagher, R.R., Gansky, S.A., and Marshall, S.J. (2000). Mechanical Properties of the Dentinoenamel Junction: AFM Studies of Nanohardness, Elastic Modulus, and Fracture. https://doi.org/10.1002/1097-4636.

7. Ho, S.P., Marshall, S.J., Ryder, M.I., and Marshall, G.W. (2007). The tooth attachment mechanism defined by structure, chemical composition and mechanical properties of collagen fibers in the periodontium. Biomaterials *28*, 5238–5245. https://doi.org/10.1016/J.BIOMATERIALS.2007.08.031.

8. Rossetti, L., Kuntz, L.A., Kunold, E., Schock, J., Müller, K.W., Grabmayr, H., Stolberg-Stolberg, J., Pfeiffer, F., Sieber, S.A., Burgkart, R., and Bausch, A.R. (2017). The microstructure and micromechanics of the tendon–bone insertion. Nat. Mater. *166.16*, 664–670. https://doi.org/10.1038/nmat4863.

9. Tits, A., and Ruffoni, D. (2021). Joining soft tissues to bone: Insights from modeling and simulations. Bone Rep. *14*, 100742. https://doi.org/10.1016/j.bonr.2020.100742.

10. Pitta Kruize, C., Panahkhahi, S., Putra, N.E., Diaz-Payno, P., Van Osch, G., Zadpoor, A.A., and Mirzaali, M.J. (2023). Biomimetic Approaches for the Design and Fabrication of Bone-to-Soft Tissue Interfaces. ACS Biomater. Sci. Eng. *9*, 3810–3831. https://doi.org/10.1021/ACSBIOMATERIALS.1C00620.

11. Waite, J.H., Lichtenegger, H.C., Stucky, G.D., and Hansma, P. (2004). Exploring Molecular and Mechanical Gradients in Structural Bioscaffolds. Biochemistry *43*, 7653–7662. https://doi.org/10.1021/BI049380H.

12. Studart, A.R. (2013). Biological and Bioinspired Composites with Spatially Tunable Heterogeneous Architectures. Adv. Funct. Mater. *23*, 4423–4436. https://doi.org/10.1002/adfm.201300340.

13. Adams, R.D., Coppendale, J., and Peppiatt, N.A. (1978). Stress Analysis of Axisymmetric Butt Joints Loaded in Torsion and Tension*13*, pp. 1–10. https://doi.org/10.1243/03093247V131001.

14. Balokhonov, R., and Romanova, V. (2019). ON THE PROBLEM OF STRAIN LOCALIZATION AND FRACTURE SITE PREDICTION IN MATERIALS WITH IRREGULAR GEOMETRY OF INTERFACES. FU. Mech. Eng. *17*, 169–180. https://doi.org/10.22190/FUME190312023B.

15. Saleh, M.N., Saeedifar, M., Zarouchas, D., and De Freitas, S.T. (2020). Stress analysis of double-lap bi-material joints bonded with thick adhesive. Int. J. Adhesion Adhes. *97*, 102480. https://doi.org/10.1016/J.IJADHADH.2019.102480.

16. Lopes Fernandes, R., Teixeira de Freitas, S., Budzik, M.K., Poulis, J.A., and Benedictus, R. (2020). Role of adherend material on the fracture of bi-material composite bonded joints. Compos. Struct. *252*, 112643. https://doi.org/10.1016/J.COMPSTRUCT.2020.112643.

17. Pei, E., Kabir, I.R., Godec, D., Gonzalez-Gutierrez, J., and Nordin, A. (2021). Functionally graded additive manufacturing. Addit. Manuf. with Funct. Nanomater. 35–54. https://doi.org/10.1016/B978-0-12-823152-4.00006-5.

18. Gao, W., Zhang, Y., Ramanujan, D., Ramani, K., Chen, Y., Williams, C.B., Wang, C.C., Shin, Y.C., Zhang, S., and Zavattieri, P.D. (2015). The status, challenges, and future of additive manufacturing in engineering. CAD Comput. Aided Des. *69*, 65–89. https://doi.org/10.1016/j.cad.2015.04.001.

19. Bakarich, S.E., Gorkin, R., Gately, R., Naficy, S., Sina in het Panhuis, M., and Spinks, G.M. (2017). 3D printing of tough hydrogel composites with spatially varying materials properties. Addit. Manuf. *14*, 24–30. https://doi.org/10.1016/j.addma.2016.12.003.

20. Kokkinis, D., Bouville, F., and Studart, A.R. (2018). 3D Printing of Materials with Tunable Failure via Bioinspired Mechanical Gradients. Adv. Mater. *30*, 1705808. https://doi.org/10.1002/ADMA.201705808.

21. Ren, L., Song, Z., Liu, H., Han, Q., Zhao, C., Derby, B., Liu, Q., and Ren, L. (2018). 3D printing of materials with spatially non-linearly varying properties. Mater. Des. *156*, 470–479. https://doi.org/10.1016/J.MATDES.2018.07.012.

22. Nguyen, D.T., Yee, T.D., Dudukovic, N.A., Sasan, K., Jaycox, A.W., Golobic, A.M., Duoss, E.B., Dylla-Spears, R., Nguyen, D.T., Yee, T.D., et al. (2019). 3D Printing of Compositional Gradients Using the Microfluidic Circuit Analogy. Adv. Mater. Technol. *4*, 1900784. https://doi.org/10.1002/ADMT.201900784.

23. Hasanov, S., Gupta, A., Nasirov, A., and Fidan, I. (2020). Mechanical characterization of functionally graded materials produced by the fused filament fabrication process. J. Manuf. Process. *58*, 923–935. https://doi.org/10.1016/J.JMAPRO.2020.09.011.

24. Salcedo, E., Baek, D., Berndt, A., and Ryu, J.E. (2018). Simulation and validation of three dimension functionally graded materials by material jetting. Addit. Manuf. *22*, 351–359.

https://doi.org/10.1016/J.ADDMA.2018.05.027.

25. Skylar-Scott, M.A., Mueller, J., Visser, C.W., and Lewis, J.A. (2019). Voxelated soft matter via multimaterial multinozzle 3D printing. Nature *575*, 330–335. https://doi.org/10.1038/s41586-019-1736-8.

26. Kumar, R., Ranjan, R., Jeyaraman, M., and Kumar, S. (2020). Inverse-designed spinodoid metamaterials. J. Orthop. Case Rep. *10*, 1–6. https://doi.org/10.1038/s41524-020-0341-6.

27. Doubrovski, E.L., Tsai, E.Y., Dikovsky, D., Geraedts, J.M.P., Herr, H., and Oxman, N. (2015). Voxel-based fabrication through material property mapping: A design method for bitmap printing. CAD Comput. Aided Des. *60*, 3–13. https://doi.org/10.1016/j.cad.2014.05.010.

28. Bader, C., Kolb, D., Weaver, J.C., Sharma, S., Hosny, A., Costa, J., and Oxman, N. (2018). Making data matter: Voxel printing for the digital fabrication of data across scales and domains. Sci. Adv. *4*, eaas8652. https://doi.org/10.1126/sciadv.aas8652.

29. Gu, G.X., Dimas, L., Qin, Z., and Buehler, M.J. (2016). Optimization of Composite Fracture Properties: Method, Validation, and Applications. J. Appl. Mech. *83*. https://doi.org/10.1115/1.4033381.

30. Abueidda, D.W., Almasri, M., Ammourah, R., Ravaioli, U., Jasiuk, I.M., and Sobh, N.A. (2019). Prediction and optimization of mechanical properties of composites using convolutional neural networks. Compos. Struct. *227*, 111264. https://doi.org/10.1016/j.compstruct.2019.111264.

31. Mirzaali, M.J., Cruz Saldívar, M., Herranz de la Nava, A., Gunashekar, D., Nouri-Goushki, M., Doubrovski, E.L., and Zadpoor, A.A. (2020). Multi-Material 3D Printing of Functionally Graded Hierarchical Soft–Hard Composites. Adv. Eng. Mater. *22*, 1901142. https://doi.org/10.1002/adem.201901142.

32. Mirzaali, M.J., Herranz de la Nava, A., Gunashekar, D., Nouri-Goushki, M., Veeger, R.P.E., Grossman, Q., Angeloni, L., Ghatkesar, M.K., Fratila-Apachitei, L.E., Ruffoni, D., et al. (2020). Mechanics of bioinspired functionally graded soft-hard composites made by multi-material 3D printing. Compos. Struct. *237*, 111867. https://doi.org/10.1016/J.COMPSTRUCT.2020.111867.

33. Saldivar, M.C., Shen, E.T.W., Doubrovski, E.L., Mirzaali, M.J., and Zadpoor, A.A. (2022). Bioinspired Rational Design of Multi-Material 3D Printed Soft-Hard Interfaces. https://doi.org/10.48550/arxiv.2206.13615.

34. Saldívar, M.C., Doubrovski, E.L., Mirzaali, M.J., and Zadpoor, A.A. (2022). Nonlinear coarse-graining models for 3D printed multi-material biomimetic composites. Addit. Manuf. *58*, 103062. https://doi.org/10.1016/J.ADDMA.2022.103062.

35. Meisel, N.A., Dillard, D.A., and Williams, C.B. (2018). Impact of material concentration and distribution on composite parts manufactured via multi-material jetting. Rapid Prototyp. J. *24*, 872–879. https://doi.org/10.1108/RPJ-01-2017-0005/FULL/PDF.

36. De Noni, L., Zorzetto, L., Briatico-Vangosa, F., Rink, M., Ruffoni, D., and Andena, L. (2022). Modelling the interphase of 3D printed photo-cured polymers. Compos. Part B Eng. *234*, 109737. https://doi.org/10.1016/J.COMPOSITESB.2022.109737.

37. Aghaei, A., Bochud, N., Rosi, G., Grossman, Q., Ruffoni, D., and Naili, S. (2022). Ultrasound characterization of bioinspired functionally graded soft-to-hard composites: Experiment and modeling. J. Acoust. Soc. Am. *151*, 1490. https://doi.org/10.1121/10.0009630.

38. Shellard, A., and Mayor, R. (2021). Durotaxis: The Hard Path from In Vitro to In Vivo. Dev. Cell *56*, 227–239. https://doi.org/10.1016/J.DEVCEL.2020.11.019.

39. Isomursu, A., Park, K.-Y., Hou, J., Cheng, B., Mathieu, M., Shamsan, G.A., Fuller, B., Kasim, J., Mahmoodi, M.M., Lu, T.J., et al. (2022). Directed cell migration towards softer environments. Nat. Mater. *21*, 1081–1090. https://doi.org/10.1038/s41563-022-01294-2.

40. Kawano, T., and Kidoaki, S. (2011). Elasticity boundary conditions required for cell mechanotaxis on microelastically-patterned gels. Biomaterials *32*, 2725–2733. https://doi.org/10.1016/J.BIOMATERIALS.2011.01.009.

41. Charras, G., and Sahai, E. (2014). Physical influences of the extracellular environment on cell migration. Nat. Rev. Mol. Cell Biol. *1512.15*, 813–824. https://doi.org/10.1038/nrm3897.

42. Shirke, P.U., Goswami, H., Kumar, V., Shah, D., Beri, S., Das, S., Bellare, J., Mayor, S., Venkatesh, K.V., Seth, J.R., and Majumder, A. (2021). Viscotaxis"- directed migration of mesenchymal stem cells in response to loss modulus gradient. Acta Biomater. *135*, 356–367. https://doi.org/10.1016/J.ACTBIO.2021.08.039.

43. Zorzetto, L., Andena, L., Briatico-Vangosa, F., De Noni, L., Thomassin, J.M., Jérôme, C., Grossman, Q., Mertens, A., Weinkamer, R., Rink, M., and Ruffoni, D. (2020). Properties and role of interfaces in multimaterial 3D printed composites. Sci. Rep. *10*, 22285. https://doi.org/10.1038/s41598-020-79230-0.

44. Helgason, B., Perilli, E., Schileo, E., Taddei, F., Brynjólfsson, S., and Viceconti, M. (2008). Mathematical relationships between bone density and mechanical properties: A literature review. Clin. Biomech. *23*, 135–146. https://doi.org/10.1016/j.clinbiomech.2007.08.024.

45. Maganaris, C.N., and Paul, J.P. (1999). In vivo human tendon mechanical properties. J. Physiol. *521 Pt 1*, 307–313. https://doi.org/10.1111/J.1469-7793.1999.00307.X.

46. Mirzaali, M.J., Schwiedrzik, J.J., Thaiwichai, S., Best, J.P., Michler, J., Zysset, P.K., and Wolfram, U. (2016). Mechanical properties of cortical bone and their relationships with age, gender, composition and microindentation properties in the elderly. Bone *93*, 196–211. https://doi.org/10.1016/j.bone.2015.11.018.

47. Mirzaali, M.J., Mussi, V., Vena, P., Libonati, F., Vergani, L., and Strano, M. (2017). Mimicking the loading adaptation of bone microstructure with aluminum foams. Mater. Des. *126*, 207–218. https://doi.org/10.1016/j.matdes.2017.04.039.

48. Nielsen, L.E., Wre, L.A., C, and Nielsen, E. (1970). Generalized Equation for the Elastic Moduli of Composite Materials. J. Appl. Phys. *41*, 4626–4627. https://doi.org/10.1063/1.1658506.

49. Counto, U.J. (1964). The Effect of the Elastic Modulus of the Aggregate on the Elastic Modulus, Creep and Creep Recovery of Concrete, pp. 129–138. https://doi.org/10.1680/macr.1964.16.48.129 16.

50. Davies, W.E.A. (1971). The theory of elastic composite materials. J. Phys. D Appl. Phys. *4*, 1325–1339. https://doi.org/10.1088/0022-3727/4/9/313.

51. Tits, A., Blouin, S., Rummler, M., Kaux, J.F., Drion, P., van Lenthe, G.H., Weinkamer, R., Hartmann, M.A., and Ruffoni, D. (2023). Structural and functional heterogeneity of mineralized fibrocartilage at the Achilles tendon-bone insertion. Acta Biomaterialia *166*, 409–418. https://doi.org/10.1016/j.actbio.2023.04.018.

52. Genin, G.M., Kent, A., Birman, V., Wopenka, B., Pasteris, J.D., Marquez, P.J., and Thomopoulos, S. (2009). Functional Grading of Mineral and Collagen in the Attachment of Tendon to. Biophys. J. *97*, 976–985. https://doi.org/10.1016/J.BPJ.2009.05.043.

53. Waite, J.H., Vaccaro, E., Sun, C., and Lucas, J.M. (2002). Elastomeric gradients: a hedge against stress concentration in marine holdfasts? Philos. Trans. R. Soc. Lond. B Biol. Sci. *357*, 143–153. https://doi.org/10.1098/RSTB.2001.1025.

54. Liu, F., Li, T., Jiang, X., Jia, Z., Xu, Z., and Wang, L. (2020). The effect of material mixing on interfacial stiffness and strength of multi-material additive manufacturing. Addit. Manuf. *36*, 101502. https://doi.org/10.1016/J.ADDMA.2020.101502.

55. Abueidda, D.W., Bakir, M., Abu Al-Rub, R.K., Bergström, J.S., Sobh, N.A., and Jasiuk, I. (2017). Mechanical properties of 3D printed polymeric cellular materials with triply periodic minimal surface architectures. Mater. Des. *122*, 255–267. https://doi.org/10.1016/j.matdes.2017.03.018.

56. Jin, Z., Zhang, Z., Demir, K., and Gu, G.X. (2020). Machine Learning for Advanced Additive Manufacturing. Matter *3*, 1541–1556. https://doi.org/10.1016/j.matt.2020.08.023.

57. Martino, F., Perestrelo, A.R., Vinarský, V., Pagliari, S., and Forte, G. (2018). Cellular mechanotransduction: From tension to function. Front. Physiol. *9*, 378185. https://doi.org/10.3389/FPHYS.2018.00824/BIBTEX.

58. Chen, Y.W., Fang, H.Y., Shie, M.Y., and Shen, Y.F. (2019). The mussel-inspired assisted apatite mineralized on PolyJet material for artificial bone scaffold. Int. J. Bioprint. *5*, 197–288. https://doi.org/10.18063/IJB.V5I2.197.

59. Currens, E.R., Armbruster, M.R., Castiaux, A.D., Edwards, J.L., and Martin, R.S. (2022). Evaluation and optimization of PolyJet 3D-printed materials for cell culture studies. Anal. Bioanal. Chem. *414*, 3329–3339. https://doi.org/10.1007/S00216-022-03991-Y/FIGURES/5.

60. Rimington, R.P., Capel, A.J., Player, D.J., Bibb, R.J., Christie, S.D.R., and Lewis, M.P. (2018).

Feasibility and Biocompatibility of 3D-Printed Photopolymerized and Laser Sintered Polymers for Neuronal, Myogenic, and Hepatic Cell Types. Macromol. Biosci. *18*, 1800113. https://doi.org/10.1002/MABI.201800113.

61. Ngan, C.G.Y., O'Connell, C.D., Blanchard, R., Boyd-Moss, M., Williams, R.J., Bourke, J., Quigley, A., McKelvie, P., Kapsa, R.M.I., and Choong, P.F.M. (2019). Optimising the biocompatibility of 3D printed photopolymer constructs in vitro and in vivo. Biomed. Mater. *14*, 035007. https://doi.org/10.1088/1748-605X/AB09C4.

62. Wells, R.G. (2008). The role of matrix stiffness in regulating cell behavior. Hepatology *47*, 1394–1400. https://doi.org/10.1002/HEP.22193.

63. Wang, T., Nanda, S.S., Papaefthymiou, G.C., and Yi, D.K. (2020). Mechanophysical Cues in Extracellular Matrix Regulation of Cell Behavior. Chembiochem *21*, 1254–1264. https://doi.org/10.1002/CBIC.201900686.

64. Urciuoli, E., and Peruzzi, B. (2020). Involvement of the FAK Network in Pathologies Related to Altered Mechanotransduction. Int. J. Mol. Sci. *21*, 9426. https://doi.org/10.3390/IJMS21249426.

65. Cornillon, J., Campos, L., Guyotat, D., Cornillon, J., Campos, L., and Guyotat, D. (2003). Focal adhesion kinase (FAK), une protéine aux fonctions multiples. Med. Sci. *19*, 743–752. https://doi.org/10.1051/MEDSCI/20031967743.

66. Du, J., Zu, Y., Li, J., Du, S., Xu, Y., Zhang, L., Jiang, L., Wang, Z., Chien, S., and Yang, C. (2016). Extracellular matrix stiffness dictates Wnt expression through integrin pathway. Sci. Rep. *6*, 20395. https://doi.org/10.1038/srep20395.

67. Matellan, C., and Del Río Hernández, A.E. (2019). Engineering the cellular mechanical microenvironment – From bulk mechanics to the nanoscale. J. Cell Sci. *132*, jcs229013. https://doi.org/10.1242/JCS.229013/57462.

68. Dupont, S., Morsut, L., Aragona, M., Enzo, E., Giulitti, S., Cordenonsi, M., Zanconato, F., Le Digabel, J., Forcato, M., Bicciato, S., et al. (2011). Role of YAP/TAZ in mechanotransduction. Nature *474*, 179–183. https://doi.org/10.1038/NATURE10137.

69. Brusatin, G., Panciera, T., Gandin, A., Citron, A., and Piccolo, S. (2018). Biomaterials and engineered microenvironments to control YAP/TAZ-dependent cell behaviour. Nat. Mater. *17*, 1063–1075. https://doi.org/10.1038/S41563-018-0180-8.

70. Totaro, A., Panciera, T., and Piccolo, S. (2018). YAP/TAZ upstream signals and downstream responses. Nat. Cell Biol. *208.20*, 888–899. https://doi.org/10.1038/s41556-018-0142-z.

71. Caliari, S.R., Vega, S.L., Kwon, M., Soulas, E.M., and Burdick, J.A. (2016). Dimensionality and spreading influence MSC YAP/TAZ signaling in hydrogel environments. Biomaterials *103*, 314–323. https://doi.org/10.1016/J.BIOMATERIALS.2016.06.061.

72. Lo, C.M., Wang, H.B., Dembo, M., and Wang, Y.L. (2000). Cell Movement Is Guided by the Rigidity of the Substrate. Biophys. J. *79*, 144–152. https://doi.org/10.1016/S0006-3495(00)76279-5.

73. Engler, A.J., Sen, S., Sweeney, H.L., and Discher, D.E. (2006). Matrix Elasticity Directs Stem Cell Lineage Specification. Cell *126*, 677–689. https://doi.org/10.1016/J.CELL.2006.06.044.

74. Kohn, J.C., and Ebenstein, D.M. (2013). Eliminating adhesion errors in nanoindentation of compliant polymers and hydrogels. J. Mech. Behav. Biomed. Mater. *20*, 316–326. https://doi.org/10.1016/J.JMBBM.2013.02.002.

75. Oliver, W.C., and Pharr, G.M. (1992). An improved technique for determining hardness and elastic modulus using load and displacement sensing indentation experiments. J. Mater. Res. *7*, 1564–1583. https://doi.org/10.1557/JMR.1992.1564.

76. ASTM D638 (2004) (ASTM Stand), ASTM D638 - 14 Standard Test Method for Tensile Properties of Plastics. https://www.astm.org/Standards/D638.

77. Knee, Joint., (2020). https://www.thingiverse.com/thing:4283166/attribution_card.

78. Zhou, S.H., McCarthy, I.D., McGregor, A.H., Coombs, R.R., and Hughes, S.P. (2000). Geometrical dimensions of the lower lumbar vertebrae – analysis of data from digitised CT images. Eur. Spine J. *93.9*, 242–248. https://doi.org/10.1007/S005860000140.